then carefully removed and prepared for microscopic examination of ink perfusion on undecalcified sections. All other specimens were harvested and fixed in 4% paraformaldehyde (pH 7.4) at 4°C for 24 h.

*Tissue engineering of bone using IP-CHA integrated with vascular bundle*

In the second set of experiments, we investigated whether vascular bundle insertion enhances new bone

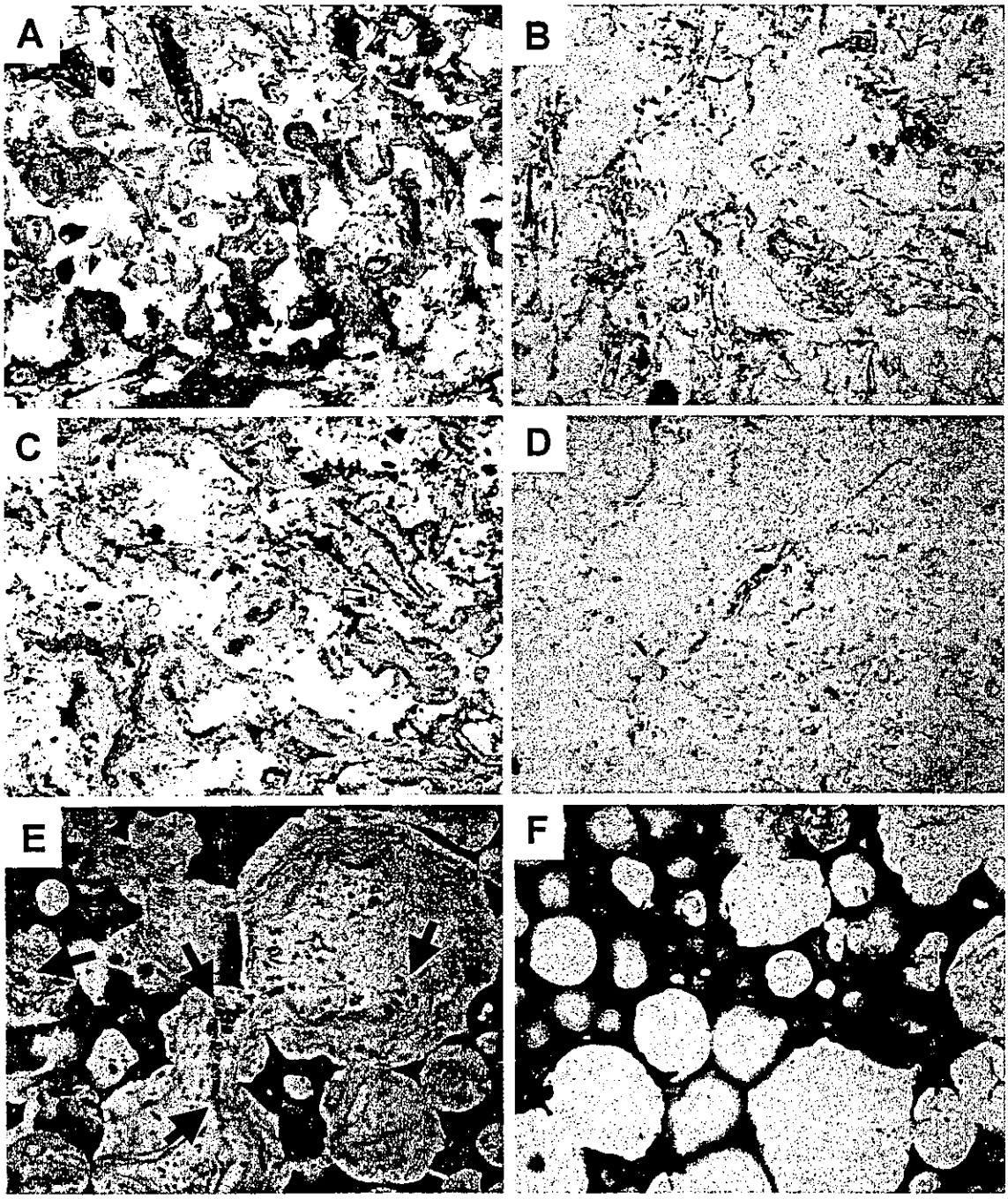


**FIG. 2.** Representative photomicrographs of IP-CHA 6 weeks after subcutaneous implantation with (**A**, **C**, and **E**) or without (**B**, **D**, and **F**) vascular bundle insertion. (**A** and **B**) Hematoxylin and eosin-stained sections (original magnification, ×100). (**A**) In IP-CHA with vascular bundle insertion, many thick blood vessels accompanied by active fibrous connective tissue formation were observed in the pores. (**B**) In the control IP-CHA group, loose fibrous tissues with microvessels were seen in the pores close to the peripheral surface of the block, but not in the deep pores. (**C** and **D**) Immunostaining for von Willebrand factor (original magnification, ×100). Note abundant thick vessels in IP-CHA with vascular bundle insertion (**C**). (**E** and **F**) Toluidine blue staining of hard tissue sections after India ink perfusion. In IP-CHA with vascular bundle insertion, thick blood vessels containing India ink were observed (**E**, arrows).

formation in tissue-engineered bone. The four rats in the vascularized BMP/IP-CHA group received an IP-CHA implant with vascular insertion loaded with 10 $\mu$g of rhBMP-2. The four rats in the control BMP/IP-CHA group were implanted with an IP-CHA block without vascular insertion loaded with 10 $\mu$g of rhBMP-2. Similarly, 10 rats were implanted with an IP-CHA block loaded with 2 $\mu$g of rhBMP-2: 5 rats with vascular insertion, and 5 rats without vascular insertion. Three weeks after implantation, all implants were removed and prepared for histological examination.

### *Histological examination*

For undecalcified sections, tissue samples were fixed in 70% ethanol for 48 h, dehydrated, and then embedded in polymethyl methacrylate. Sections (6 $\mu$m thick) along the drill hole were then made, and were stained with toluidine blue for assessment of histological details.

All other tissue samples were decalcified in 20% EDTA (pH 7.4) at 4°C, dehydrated, and then embedded in paraffin. Each sample was cut into 5 $\mu$m sections along the drill hole; these were processed for further study. Hematoxylin–eosin staining was used to examine details of tissue in the pores. To visualize vessels in the pores, immunohistochemical staining using anti-von Willebrand factor antibody was performed as described previously.[14]

### *Quantification of bone formation in the pores*

For quantitative assessment of bone formation in the pores of BMP/IP-CHA implants, the hematoxylin–eosin-stained cross-section of the implant (length, 10 mm) was subdivided into three zones of equal width. The gross area of newly formed bone matrix in the central third of the cross-section was measured with a computer-assisted image analyzer (WinRoof; Mitani, Fukui, Japan).

### *Statistical analysis*

Statistical significance of differences was analyzed by unpaired $t$ test, using the statistical program StatView (version 5.0; SAS, Cary, NC). A $p$ value of $<0.05$ was considered to indicate statistical significance.

## RESULTS

### *Development of vascular network in the pores of IP-CHA*

In all rats in the vascularized IP-CHA group, the inserted vascular pedicles displayed firm pulsation at the entrance of the IP-CHA block (Fig. 1, arrowhead). India ink perfusion produced dark stains on all surfaces of IP-CHA blocks, suggesting abundant blood flow from the pedicle inside the block to its outer surface. In contrast, in all animals in the control IP-CHA group, the surface of the implanted block was not stained by India ink.

In histological examination of the longitudinal cross-sections of the IP-CHA blocks, in the vascularized IP-CHA group, we observed many large blood vessels, which appeared to originate from the inserted vascular bundle, in the pores throughout the IP-CHA block. In the India ink perfusion experiment, most of the vessels in the pores of the vascularized IP-CHA group contained black ink particles, indicating that those vessels were effectively connected to the host circulation via the inserted vascular pedicle, providing an abundant blood supply (Fig. 2A, C, and E).

In the control IP-CHA group, fibrous tissues with microvessels were observed in the pores close to the outer surface of the block, but not in the deep pores. Furthermore, compared with the vascularized IP-CHA group, the fibrous tissues seen in the control IP-CHA group were markedly looser and the vessels were more immature and smaller. In those small vessels, very little India ink was seen, suggesting poor blood supply (Fig. 2B, D, and F).

In the vascularized IP-CHA group, immunostaining for von Willebrand factor clearly visualized blood vessels in almost every pore, suggesting a well-developed vascular network in the IP-CHA pores, due in part to interpore connections (Fig. 2C).

### *Effect of vascular bundle insertion on BMP-induced bone formation in IP-CHA*

Histological examination of the longitudinal cross-sections of IP-CHA blocks loaded with 10 $\mu$g of rhBMP-2 showed that, in the vascularized BMP/IP-CHA group, there was abundant newly formed bone tissue in the pores. New bone formation was especially abundant in the pores close to the inserted vascular bundle; that is, far from the surface of the block. That newly formed bone tissue was accompanied by many large blood vessels that appeared to derive from the inserted vascular bundle (Fig. 3A and B). In the control BMP/IP-CHA group, most of the pores were filled with loose fibrous tissue with microvessels; a small amount of newly formed bone was observed in the pores close to the surface of the block at both ends, but not in the deep portion (Fig. 3C).

The average values (±standard deviation) for gross area of newly formed bone matrix in the pores of the central third were $1.0 \pm 0.64$ mm$^2$ in the vascularized BMP/IP-CHA group and $0.046 \pm 0.054$ mm$^2$ in the control BMP/IP-CHA group. The difference between these two values was statistically significant (Fig. 3D, $p < 0.05$).

In the experiment using a lower dose of rhBMP-2 (2 $\mu$g/block), we found no bone formation in the pores of IP-CHA blocks, with or without vascular insertion.

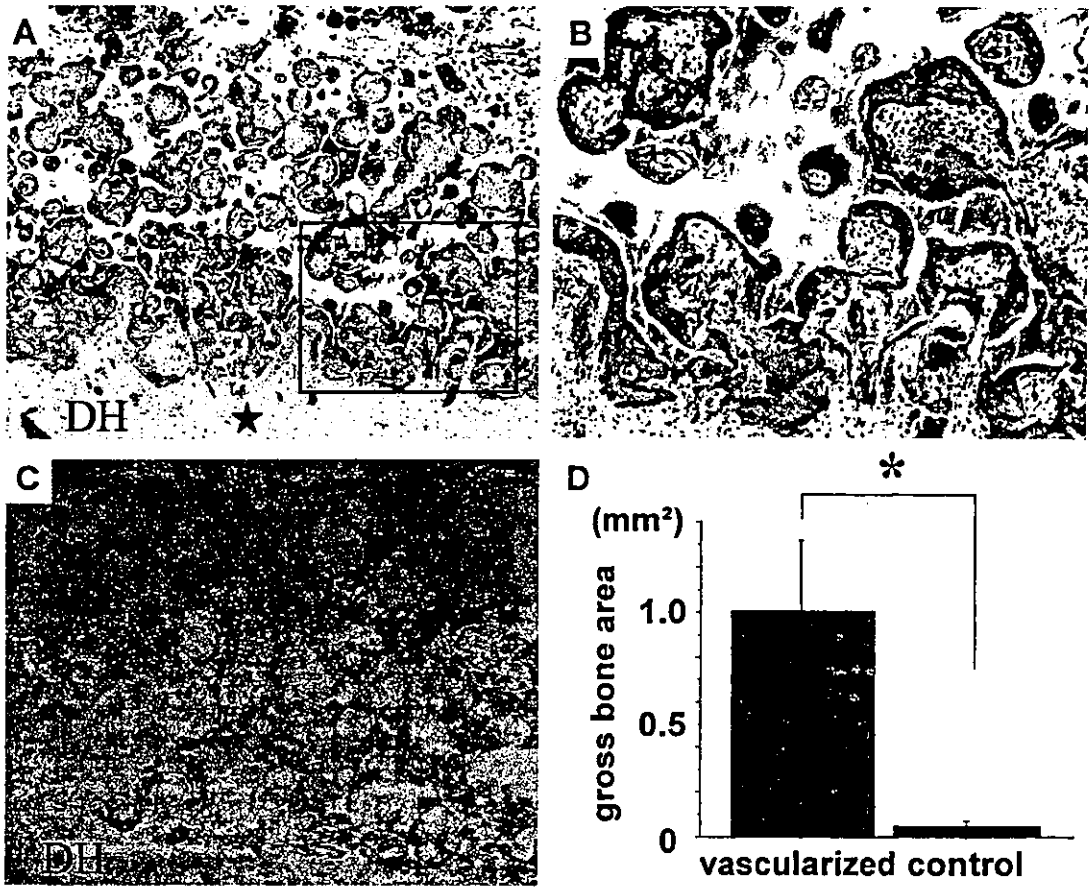


**FIG. 3.** Effect of vascular bundle insertion on bone formation in the deep portion of IP-CHA loaded with 10 $\mu$g of rhBMP-2. Representative microphotographs 3 weeks after subcutaneous implantation with (**A** and **B**) or without (**C**) vascular bundle insertion. (**A**) Abundant new bone formation with neovascularization was seen in the pores close to the longitudinal drill hole (**DH**), into which the superficial inferior epigastric vessels (star) were inserted (original magnification, ×40). (**B**) Higher magnification (×100) of the boxed area in (**A**). (**C**) Only minimal cellular invasion with microvessels was observed in the pores along the longitudinal drill hole (**DH**); no bone formation was observed (original magnification, ×40). (**D**) Histomorphometric results for the area of newly formed bone matrix in the central third of IP-CHA blocks. Vascularized, vascularized BMP/IP-CHA group (with vascular bundle insertion); control, control BMP/IP-CHA group (without vascular bundle insertion). Values represent the average area ($mm^2$) and standard deviations of four samples in each group. $*p < 0.05$.

## DISCUSSION

Although porous ceramic bone substitutes made from calcium phosphate (e.g., HA) have been widely used in surgery to repair bone defects, their application is still limited because blood supply is essential for treatment of large bone defects and those with poor blood supply. In the present study, we found that insertion of a vascular bundle into IP-CHA produced a capillary vessel network in the pores. The present results indicate that, even when IP-CHA is implanted into a bone defect site with poor blood supply, insertion of a vascular bundle produces an abundant blood supply in most of the pores directly from the inserted vessels. The use of such implants appears to improve bone regeneration in bone defect sites.

In rigorous investigations of bone tissue-engineering techniques using bone matrix-producing cells or bone-inducible factors, porous HA was found to be a particularly suitable biomaterial for use as a scaffold.[11,15–19] It has been suggested that blood supply is an important element of bone tissue engineering, but no direct evidence of this has previously been reported. The present results, obtained using BMP-2 as the bone-inducible factor and IP-CHA as the scaffold, clearly demonstrate the essential role of blood supply in bone tissue engineering. The technique used in this study can also be used for cell-based bone tissue engineering; it is reasonable to assume that blood supply also plays an important role in cell-based bone tissue engineering.

There have been several studies in which a muscle flap was used as a source of blood supply for tissue engineering of bone.[20–24] However, this technique sacrifices

normal host muscle and, for recipient sites out of reach of a muscle flap, this technique is either not possible or requires vascular anastomoses. Because the present technique does not sacrifice any functional organ (including muscle), it could be used without affecting motor system function. Furthermore, this technique could be used to treat bone defects almost anywhere in the trunk and extremities, using local vessels. For example: for the femur, the deep femoral artery/vein bundle or inferior epigastric vessels could be used; for the humerus, deep brachial vessels; for the forearm, interosseous vessels.

In conclusion, the present results demonstrate that vascular bundle insertion into IP-CHA produces a vascular network in the porous structure, and that vascular bundle insertion enhances new bone formation in tissue-engineered bone, using rhBMP-2 and IP-CHA. Although further study is needed to clarify the clinical relevance of these findings, we believe that the present system of integrating a vascular network into IP-CHA is a useful technique for bone tissue engineering as a treatment for challenging orthopedic conditions.

## ACKNOWLEDGMENTS

This work was supported in part by grants from the New Energy and Industrial Technology Development Organization (NEDO); the Ministry of Health, Labour, and Welfare, Japan; and the Ministry of Education, Culture, Sports, Science, and Technology, Japan. We thank Miss Kanae Asai for excellent technical assistance.

## REFERENCES

1. Jarcho, M. Calcium phosphate ceramics as hard tissue prosthetics. Clin Orthop **157,** 259, 1981.
2. Bucholz, R., Carlton, A., and Holmes, R. Interporous hydroxyapatite as a bone graft substitute in tibial plateau fractures. Clin. Orthop. **240,** 53, 1988.
3. Uchida, A., Araki, N., Shinto, Y., Yoshikawa, H., Kurisaki, E., and Ono, K. The use of calcium hydroxyapatite ceramic in bone tumor surgery. J. Bone Joint Surg. Br. **72,** 298, 1990.
4. Nakano, K., Harata, S., Suetsuna. F., Araki, T., and Itoh, J. Spinous process-splitting laminoplasty using hydroxyapatite spinous process spacer. Spine **17,** 41, 1992.
5. Ayers, R.A., Simske. S.J., Nunes, C.R., and Wolford, L.M. Long-term bone ingrowth and residual microhardness of porous block hydroxyapatite implants in human. J Oral Maxillofac. Surg. **56,** 1297, 1998.
6. Mori, S., Yoshikawa, H., Hashimoto, J., Ueda, T., Funai, H., Kato, M., and Takaoka, K. Antiangiogenic agent (TNP-470) inhibition of ectopic bone formation induced by bone morphogenetic protein-2. Bone **22,** 99, 1998.
7. Kusumoto, K., Bessho, K., Fujimura, K., Akioka, J., Okubo, Y., Ogawa, Y., and Iizuka, T. The effect of blood supply in muscle and an elevated muscle flap on endogenous tissue-engineered bone by rhBMP-2 in the rat. Ann. Plast. Surg. **45,** 408, 2000.
8. Fujimura, K., Bessho, K., Kusumoto, K., Konishi, Y., Ogawa, Y., and Iizuka, T. Experimental osteoinduction by recombinant human bone morphogenetic protein 2 in tissue with low blood flow: A study in rats. Br. J. Oral Maxillofac. Surg. **39,** 294, 2001.
9. Taylor, G.I., Miller, G.D.H., and Ham, F.J. The free vascularised bone graft. A clinical extension of microsurgical technique. Plast. Reconstr. Surg. **55,** 533, 1975.
10. Weiland, A.J., Moore, J.R., and Daniel, R.K. Vascularised bone autografts. Clin Orthop. **174,** 87, 1983.
11. Quarto, R., Mastrogiacomo, M., Cancedda, R., Kutepov, S.M., Mukhachev, V., Lavroukov, A., Kon, E., and Marcacci, M. Repair of large bone defects with the use of autologous bone marrow stromal cells. N. Engl. J. Med. **344,** 385, 2001.
12. Tamai, N., Myoui, A., Tomita T, Nakase, T., Tanaka, J., Ochi, T., and Yoshikawa, H. Novel hydroxyapatite ceramics with an interconnective porous structure exhibit superior osteoconductive in vivo. J. Biomed. Mater. Res. **59,** 110, 2002.
13. Saito, N., Okada, T., Horiuchi, H., Murakami, N., and Takaoka K. A biodegradable polymer as a cytokine delivery system for inducing bone formation. Nat. Biotechnol. **19,** 332, 2001.
14. Nakase, T., Kaneko, M., Tomita, T., Myoui, A., Ariga, K., Sugamoto, K., Uchiyama, Y., Ochi, T., and Yoshikawa, H. Immunohistochemical detection of cathepsin D, K, and L in the process of endochondral ossification in the human. Histochem. Cell Biol. **114,** 21, 2000.
15. Norman, M.E., Elgendy, H.M., Shors, E.C., el-Amin, S.F., and Laurencin, C.T. An *in-vitro* evaluation of coralline porous hydroxyapatite as a scaffold for osteoblast growth. Clin. Mater. **17,** 85, 1994.
16. Kon, E., Muraglia, A., Corsi, A., Bianco, P., Marcacci, M., Martin, I., Boyde, A., Ruspantini, I., Chistolini, P., Rocca, M., Giardino, R., Cancedda, R., and Quarto, R. Autologous bone marrow stromal cells loaded onto porous hydroxyapatite ceramic accelerate bone repair in critical-size defects of sheep long bones. J. Biomed. Mater. Res. **49,** 328, 2000.
17. Petite, H., Viateau, V., Bensaid, W., Meunier, A., de Pollak, C., Bourguignon, M., Oudina, K., Sedel, L., and Guillemin, G. Tissue-engineered bone regeneration. Nat Biotechnol. **18,** 959, 2000.
18. Noshi, T., Yoshikawa, T., Ikeuchi, M., Dohi, Y., Ohgushi, H., Horiuchi, K., Sugimura, M., Ichijima, K., and Yonemasu, K. Enhancement of the in vivo osteogenic potential of marrow/hydroxyapatite composites by bovine bone morphogenetic protein. J. Biomed. Mater. Res. **52,** 621, 2000.
19. Boo, J.S., Yamada, Y., Okazaki, Y., Hibino, Y., Okada, K., Hata, K., Yoshikawa, T., Sugiura, Y., and Ueda, M. Tissue-engineered bone using mesenchymal stem cells and a biodegradable scaffold. J. Craniofac. Surg. **13,** 231, 2002.
20. Bernard, S.L., and Picha, G.J. The use of coralline hydroxyapatite in a "biocomposite" free flap. Plast. Reconstr. Surg. **87,** 96, 1991.
21. Kusumoto, K., Bessho, K., Fujimura, K., Akioka, J.,

Ogawa, Y., and Iizuka, T. Prefabricated muscle flap including bone induced by recombinant bone morphogenetic protein-2: An experimental study of ectopic osteoinduction in a rat latissimus dorsi muscle flap. Br. J. Plast. Surg. **51,** 275, 1998.

22. Casabona, F., Martin, I., Muraglia, A., Berrino, P., Santi, P., Cancedda, R., and Quarto, R. Prefabricated engineered bone flaps: An experimental model of tissue reconstruction in plastic surgery. Plast. Reconstr. Surg. **101,** 577, 1998.
23. Terheyden, H., Jepsen, S., and Rueger, D.R. Mandibular reconstruction in miniature pigs with prefabricated vascularized bone grafts using recombinant human osteogenic protein-1: A preliminary study. Int. J. Oral Maxillofac. Surg. **28,** 461, 1999.
24. Alam, M.I., Asahina, I., Seto, I., Oda, M., and Enomoto, S. Prefabricated vascularized bone flap: A tissue transformation technique for bone reconstruction. Plast. Reconstr. Surg. **15,** 952, 2001.

Address reprint requests to:
*Akira Myoui, M.D.*
*Osaka University Graduate School of Medicine*
*Department of Orthopedics*
*2-2 Yamadaoka, Suita 565-0871, Japan*

*E-mail:* myoi@ort.med.osaka-u.ac.jp

*Cell Transplantation*, Vol. 13, pp. 367–376, 2004
Printed in the USA. 

0963-6897/04 $20.00 + .00


# Bone Tissue Engineering Using Novel Interconnected Porous Hydroxyapatite Ceramics Combined With Marrow Mesenchymal Cells: Quantitative and Three-Dimensional Image Analysis

Masataka Nishikawa,* Akira Myoui,* Hajime Ohgushi,† Masako Ikeuchi,†
Noriyuki Tamai,* and Hideki Yoshikawa*

*Department of Orthopaedics, Osaka University Graduate School of Medicine,
2-2 Yamadaoka, Suita City, Osaka 565-0871, Japan
†Tissue Engineering Research Center, National Institute of Advanced Industrial Science and Technology,
3-11-46 Nakouji, Amagasaki City, Hyogo 661-0974, Japan

We developed fully opened interconnected porous calcium hydroxyapatite ceramics having two different pore sizes. One has pores with an average size of 150 μm in diameter, an average 40-μm interconnecting pore diameter, and 75% porosity (HA150). The other has pores with an average size of 300 μm in diameter, an average 60–100-μm interconnecting pore diameter, and 75% porosity (HA300). Because of its smaller pore diameter, HA150 has greater mechanical strength than that of HA300. These ceramics were combined with rat marrow mesenchymal cells and cultured for 2 weeks in the presence of dexamethasone. The cultured ceramics were then implanted into subcutaneous sites in syngeneic rats and harvested 2–8 weeks after implantation. All the implants showed bone formation inside the pore areas as evidenced by decalcified histological sections and microcomputed tomography images, which enabled three-dimensional analysis of the newly formed bone and calculation of the bone volume in the implants. The bone volume increased over time. At 8 weeks after implantation, extensive bone volume was detected not only in the surface pore areas but also in the center pore areas of the implants. A high degree of alkaline phosphatase activity with a peak at 2 weeks and a high level of osteocalcin with a gradual increase over time were detected in the implants. The levels of these biochemical parameters were higher in HA150 than in HA300. The results indicate that a combination of HA150 and mesenchymal cells could be used as an excellent bone graft substitute because of its mechanical properties and capability of inducing bone formation.

Key words: Bone tissue engineering; Hydroxyapatite; Image analysis; Marrow mesenchymal cell; Osteoblast; Osteoconduction

## INTRODUCTION

The ideal bone graft is autogenous bone but there are many problems, such as quantitative limitations of the graft and the inevitable invasion of normal tissues to harvest the graft bone. To avoid these problems, synthetic hydroxyapatite (HA) ceramics have been used as bone graft substitutes in orthopedic, craniofacial, and dental applications (1,3,7,10,21). HA ceramics are known to be biocompatible, osteoconductive, and bioactive, with bone bonding directly to the surface of the ceramics (4,8,22). However, only a few researchers have reported that the pores of implanted ceramics were completely filled with the newly formed host bone (22). It would be reasonable to assume that the reason for this is the nonuniform pore geometry and few interpore connections of conventional synthetic HA ceramics. The size of the interpore connections rather than the size of the pores themselves might be the primary limiting factor of osteoconduction into the central area of HA ceramic blocks. This is because interpore connections under 3 μm in diameter do not permit cell migration and vascularization into the pores, events essential for new bone formation (20).

We recently developed fully open interconnected porous calcium hydroxyapatite ceramics (IP-CHA) and reported the resulting superior osteoconduction by permitting cells and tissues to invade deep into the pores (20). However, not all of these ceramics are osteoinductive and, therefore, the applications are limited. In this re-

Address correspondence to Hajime Ohgushi, M.D., Ph.D., Tissue Engineering Research Center, National Institute of Advanced Industrial Science and Technology, 3-11-46 Nakouji, Amagasaki City, Hyogo 661-0974, Japan. Tel: (+81) 6-6494-7806; Fax: (+81) 6-6494-7861; E-mail: hajime-ohgushi@aist.go.jp

gard, we have reported on the osteogenic capability of fresh marrow cells or culture-expanded marrow mesenchymal cells, which combined with porous HA ceramics. Such composites showed ectopic bone formation in the pore areas of the HA ceramics (11,13,14,18,24,25). Importantly, the composites also demonstrated their healing potential when implanted into a site in which there is a bony defect (12). Due to the interconnected porous structure of IP-CHA, osteogenic cells can be appropriately introduced within the pores and are thus useful as a scaffold in bone tissue engineering. In this study, IP-CHA, having two different pore sizes, were combined with marrow mesenchymal cells and evaluated for their osteogenic capability.

## MATERIALS AND METHODS

### *Materials*

Fully open IP-CHA were synthesized by adopting a "foam-gel" technique from a slurry of hydroxyapatite (60 wt%) with a cross-linking substrate (polyethyleneimine, 40 wt%), as previously reported (20). The solid and porous components of the microstructure were completely interconnected. We prepared two types of IP-CHA. One had pores averaging 150 μm in diameter, an average 40-μm interconnecting pore diameter, and 75% porosity (HA150). The other had pores averaging 300 μm in diameter, 60–100-μm interconnecting pore diameter, and 75% porosity (HA300).

For comparison, we purchased three different commercially available synthetic porous hydroxyapatite ceramics (HA-A, HA-B, and HA-C), which have been used in orthopedic or dental surgery in Japan. HA-A has an average pore diameter of 300 μm and 50% porosity. HA-B has an average pore diameter of 200 μm and 70% porosity. HA-C has pore with diameters of 50–300 μm and 35–48% porosity.

Blocks of these ceramics (HA150, HA300, HA-A, HA-B, and HA-C) were cut and shaped into 5-mm-diameter disks that were 2 mm thick.

### *Mercury Porosimetry*

The distribution of the interpore connections in hydroxyapatite ceramics was measured from the penetration of Hg liquid in an evacuated porosimeter (pore sizer, 9310, Shimadzu Co., Kyoto, Japan) as previously described by Tamai et al. (20). The available pores that were connected by interpore connection >10 μm in diameter were calculated by the following equation: available porosity (%) = total porosity (%) − unavailable porosity (%) (the inaccessible pore space calculated by integrating the cumulative volume of pores that were connected with interpore connections <10 μm in a diameter, according to the result of mercury porosimeter).

### *Marrow Cell Preparation and Culture*

Marrow cells were obtained from the bone shaft of the femora of 7-week-old Fischer 344 male rats. Both ends of the femur were cut away from the epiphysis, and the marrow was flushed out using 10 ml of culture medium expelled from a syringe through a 21-gauge needle, according to the method developed by Maniatopoulos et al. (9). The released cells were collected in two T-75 flasks (Costar, Cambridge, MA) containing 15 ml of the standard medium described below. The medium was changed after 24 h to remove hematopoietic cells. Subsequently, the medium was renewed three times a week. Cultures were maintained in a humidified atmosphere of 95% air with 5% $CO_2$ at 37°C.

The standard medium consisted of Eagle's minimal essential medium (MEM) containing 15% fetal bovine serum (JRH Bioscience, Lenexa, KS, Lot No.002095) and antibiotics (100 U/ml of penicillin, 100 μg/ml of streptomycin, and 0.25 μg/ml of amphotericin B; Sigma Chemical Co., St. Louis, MO).

After 7 days in primary culture, adherent marrow mesenchymal cells (MMCs) were released from the culture substratum using 0.1% trypsin. The cells were concentrated by centrifugation at 900 rpm for 5 min at 4°C and resuspended at $10^6$ cells/ml. The 24 ceramic disks were soaked in 4 ml of cell suspension ($10^6$ cells/ml) overnight in a $CO_2$ incubator.

After the overnight incubation, the disks were transferred into a 24-well plate (Falcon, Franklin Lakes, NJ) for subcultures. Each ceramic was subcultured in one well with 1 ml of the standard medium supplemented with 10 mM of β-glycerophosphate, disodium salt, pentahydrate (Calbiochem, Darmstadt, Germany), 82 μg/ml of L-ascorbic acid phosphate magnesium salt *n*-hydrate (Wako Pure Chemical Industrials, Osaka, Japan), and $10^{-8}$ M of dexamethasone (Dex, Sigma Chemical Co.). To evaluate the efficiency of the dexamethasone, the subcultures without Dex were used as in vitro controls. The medium was renewed three times a week, and the subcultures were maintained for 2 weeks. These subcultured MMCs in the ceramic disks were washed twice with phosphate-buffered saline (Gibco, Invitrogen Corporation, Grand Island, NY) and prepared for measurement of alkaline phosphatase (ALP) activity to evaluate if the HA ceramics support in vitro osteoblastic differentiation of marrow mesenchymal cells.

### *Implantation*

Syngeneic 7-week-old male Fischer 344 rats were anesthetized by intramuscular injection of ketamine (45 mg/kg) and xylazine (9 mg/kg). Five ceramic disks cultured with MMCs in the presence of Dex for 2 weeks were implanted subcutaneously at five sites into the back of each syngeneic rat and five ceramic disks with-

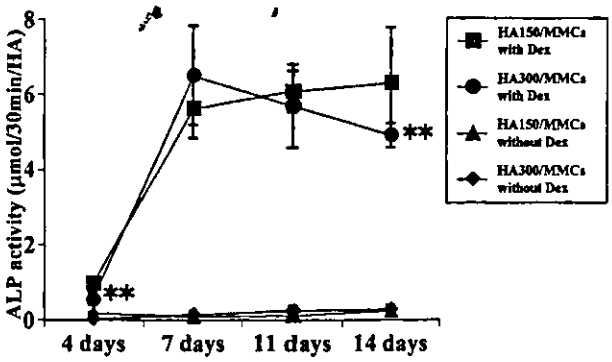


**Figure 1.** In vitro alkaline phosphatase activity (ALP) of fully open interconnected porous calcium hydroxyapatite (IP-CHA), which was combined with MMCs and cultured in the presence or absence of dexamethasone (Dex). Two types of IP-CHA, one with pores with an average diameter of 150 μm (HA150) and the other with pores with an average diameter of 300 μm (HA300), were used in this experiment as in vitro cell culture substrata. The culture was performed with or without Dex. ALP activity of four groups: HA150/MMCs with Dex, HA300/MMCs with Dex, HA150/MMCs without Dex, and HA300/MMCs without Dex. Data are presented as mean ± SD ($n = 5$). $^{**}p < 0.01$ vs. HA150/MMCs with Dex. All ALP activity in HA150/MMCs and HA300/MMCs without Dex was significantly lower than that of HA150/MMCs with Dex.

confirmed that both types of IP-CHA can maintain Dex-dependent in vitro osteoblastic differentiation of MMCs, and HA150 has more superior capabilities for supporting differentiation than does HA300.

*Histological Analyses After In Vivo Implantation*

As stated above, HA150/MMCs and HA300/MMCs can show in vitro osteoblastic differentiation under the culture condition with Dex. We also reported that the ceramic/MMCs cultured with Dex showed immediate and more copious new bone formation after in vivo implantation compared with those cultured without Dex. Therefore, we performed in vivo implantation using ceramics that were combined with MMCs and cultured for 2 weeks with Dex. After the 2-week culture, the pore surface of the ceramics could be covered with a thin layer of bone matrix together with a lining of active osteoblasts and thus we refer to these cultured ceramics as constructs (ceramics/MMCs/cult construct). As a negative control, we also implanted the ceramics without cells.

Two weeks after in vivo implantation of HA150/MMCs/cult and HA300/MMCs/cult, we were able to detect obvious bone formation in many pore areas of the ceramic (Fig. 2). Bone tissue, together with many cuboidal active osteoblasts, was observed in contact with the pore surface. Newly formed vascular vessels were also observed in some pores. This finding suggests that a capillary network had been established in the IP-CHA because of the sufficient interpore connections of the ceramics. At 8 weeks after implantation (Fig. 3A, B), the bone areas and number of osteocytes in the bone matrix increased and almost all pore areas showed bone formation. In addition, regenerated bone marrow was observed together with fat cells in many pores (Fig. 3A, B). These findings indicate the importance of porous architecture (excellent interpore connections) of IP-CHA for new bone formation. To confirm the importance of the interpore connections, we also utilized three commercially available Japanese synthetic porous hydroxyapatite ceramics (HA-A, HA-B, and HA-C). The porous architectures of these ceramics are different from IP-CHA: each pore of the commercial ceramics is not fully interconnected and have many isolated porous areas or dead-end pores. These three ceramics (HA-A, HA-B, and HA-C) were combined with MMCs and cultured with Dex for 2 weeks to make constructs of HA-A/MMCs/cult, HA-B/MMCs/cult, and HA-C/MMCs/cult. These constructs were implanted at subcutaneous sites for 8 weeks and harvested. The culture/implantation methods were the same as those applied for the constructs of HA150/MMCs/cult and HA300/MMCs/cult. In contrast to IP-CHA (Fig. 3A, B), only a few pore areas in these constructs showed newly formed bone (Fig. 3C–E). Furthermore, some pore areas did not show any newly formed tissue and were empty. Therefore, ceramics having full interpore connections (HA150 and HA300) cultured with MMCs have superior in vivo bone-forming capabilities in comparison with other ceramics (HA-A, HA-B, and HA-C) with MMCs.

Although the constructs of HA150/MMCs/cult and HA300/MMCs/cult had excellent osteogenic properties, the ceramics not combined with the cells formed only fibrovascular tissue and there was no evidence of bone formation in the pore areas of the ceramics (Fig. 4).

*Biochemical Analyses After In Vivo Implantation*

Histological analyses showed the in vivo osteogenic capacity of the constructs of HA150/MMCs/cult and HA-300/MMCs/cult and nonosteogenic capacity of the IP-CHA (HA150 and HA300) without MMCs. To demonstrate the quantitative analyses of the osteogenic capacity, we measured ALP activity as well as the osteocalcin contents of the implants, because ALP is known to localize on the cellular membrane of active osteoblasts and osteocalcin is the bone-specific protein produced exclusively by osteoblasts.

High levels of ALP activities could be detected in both the constructs of HA150/MMCs/cult and HA300/MMCs/cult. Both showed a peak in activity 2 weeks after implantation followed by a decrease. However, the levels of activity in HA150/MMCs/cult at 4 and 6 weeks

out MMCs were also implanted as controls. The rats were sacrificed at 2, 4, 6, and 8 weeks after implantation, and the implants were harvested from each experimental group for biochemical and histological assay. All procedures used in the animal experiments complied with the standards given in the Osaka University Medical School Guidelines for the Care and Use of Laboratory Animals.

*Histological Examination*

To obtain decalcified sections, 5 implants harvested from each group at 2, 4, 6, and 8 weeks were fixed in 10% buffered formalin, decalcified with K-CX solution (Falma Co., Tokyo, Japan), and embedded in paraffin. They were cut parallel to the round face of the implants and were stained with hematoxylin and eosin for light microscopy.

*Biochemical Analysis*

ALP activity was measured as reported previously (24). Each ceramic disk was crushed, homogenized in 0.2% Nonidet P-40 containing 1 mM $MgCl_2$, and centrifuged at 10,000 rpm for 1 min at 4°C. Then the supernatant was assayed for ALP using *p*-nitrophenyl phosphate as a substrate. ALP activity was represented as μmol of *p*-nitrophenol released per ceramic disk for 30 min of incubation at 37°C (19).

Osteocalcin was extracted from the sediment after extraction of 20% formic acid for 2 weeks at 4°C. An aliquot (1 ml) of the formic acid extract was then applied to a column of NAP-10 (Sephadex G-25 DNA grade, Amersham Bioscience, Uppsala, Sweden) and was eluted with 1.5 ml of 10% formic acid. Protein fractions were collected, lyophilized, and prepared for the assay of intact rat osteocalcin as previously described (6). The assay method (Rat Osteocalcin EIA Kit; No. BT-490 Biomedical Technologies Inc., Stoughton, MA) utilized two antibodies that recognized the N-and C-terminal amino acid regions of rat osteocalcin. Purified rat osteocalcin was used for standard and tracer.

*Microcomputed Tomography Evaluation*

Bone formed in the pore areas of the ceramics was evaluated by microcomputed tomography [micro-CT: MCT-CB100MF(Z); Hitachi Medical Corporation, Tokyo, Japan]. After fixation in 10% buffered formalin, each implant was placed as a round face facing the jig surface and scanned at intervals of every 10 μm at a voltage of 50 kV, 200 μA. The analytical condition was superprecision mode and 7× magnification with an image intensifier field of 1.8 in. After the samples were scanned, they were decalcified and prepared for the histological sections. The micro-CT image at almost the same level as the histological section was compared and the intensity of the newly formed bone in the micro-CT image was determined. Then the newly formed bone areas in the micro-CT images that matched with the histology were extracted and their volumes were measured using the software package, TRI3D-BON (Ratoc System Engineering Co., Ltd., Tokyo, Japan).

*Statistical Analysis*

Statistical analysis was performed using unpaired *t*-test with statistical analysis software, STATVIEW version 4.5 (SAS Institute Inc., Cary, NC). The statistical significance level was set at $p = 0.05$.

## RESULTS

*Evaluation of Interconnected Porosity*

The distribution of the interpore connections was measured using mercury porosimetry technique. In IP-CHA, most of the interpore connections ranged from 10 to 100 μm in diameter, a dimension that theoretically would be permissive to cell migration or tissue invasion from pore to pore. The interpore connections of HA150 and HA300 had a maximum peak at 40 and 80 μm, respectively. Interpore connections >10 μm accounted for as much as 90% of the total porosities in IP-CHA. The available porosities of HA150 and HA300 were as high as 67% and 70%, respectively. However, in HA-A, HA-B, and HA-C, the maximum peaks of the interpore connections were at 22, 15, and <1 μm, respectively. In addition, the total number of the interpore connections was much less than IP-CHA. The available porosities of HA-A, HA-B, and HA-C were as low as 28.5%, 36.7%, and 2.5%.

*In Vitro Osteoblastic Differentiation of MMCs*

It is well known that MMCs can differentiate into osteoblasts in culture conditions with Dex (9,15). We also reported that in vitro osteoblastic differentiation can occur on the surface of many kinds of ceramics (16,17). As a result of these findings, we first examined whether the fully open interconnected porous calcium hydroxyapatite ceramics (IP-CHA) can support in vitro differentiation by measuring ALP, one of the osteoblastic markers. IP-CHA (HA150 and HA300), having two different pore sizes, were combined with MMCs and then cultured for 2 weeks in the presence or absence of Dex. As shown in Figure 1, the ALP activities of HA150 with MMCs (HA150/MMCs) and that of HA300 with MMCs (HA300/MMCs) cultured with Dex were considerably higher than those cultured without Dex throughout the culture period. The fluctuation of ALP activities of HA150/MMCs and HA300/MMCs with Dex during the culture period showed a similar pattern, but the activity of HA150/MMCs was higher than that of HA300/MMCs at 4 and 14 days after culture. These findings

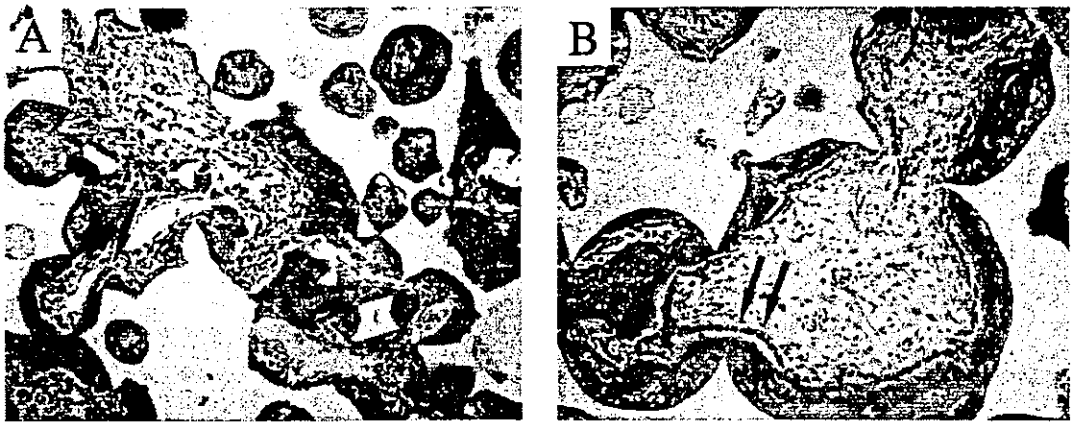


**Figure 2.** Histology of 2-week in vivo implanted IP-CHA construct, which was combined with MMCs and cultured with Dex. (A) The HA150/MMCs/cult construct and (B) HA300/MMCs/cult construct 2 weeks after implantation. The white area is the ghost of hydroxyapatite ceramic produced by decalcification; the black area is the bone formed in the ceramic pore areas. The arrows indicate active osteoblasts forming bone. Hematoxylin and eosin staining; original magnification ×100.

after implantation were higher than those in HA300/MMCs/cult (Fig. 5). Thus, the decrease was more evident in HA300/MMCs/cult than in HA150/MMCs/cult. The osteocalcin contents could be detected at 2 weeks after implantation of both constructs, followed by a steady increase over time. During this time, the contents of osteocalcin in HA150/MMCs/cult were always significantly higher than in HA300/MMCs/cult (Fig. 6). In

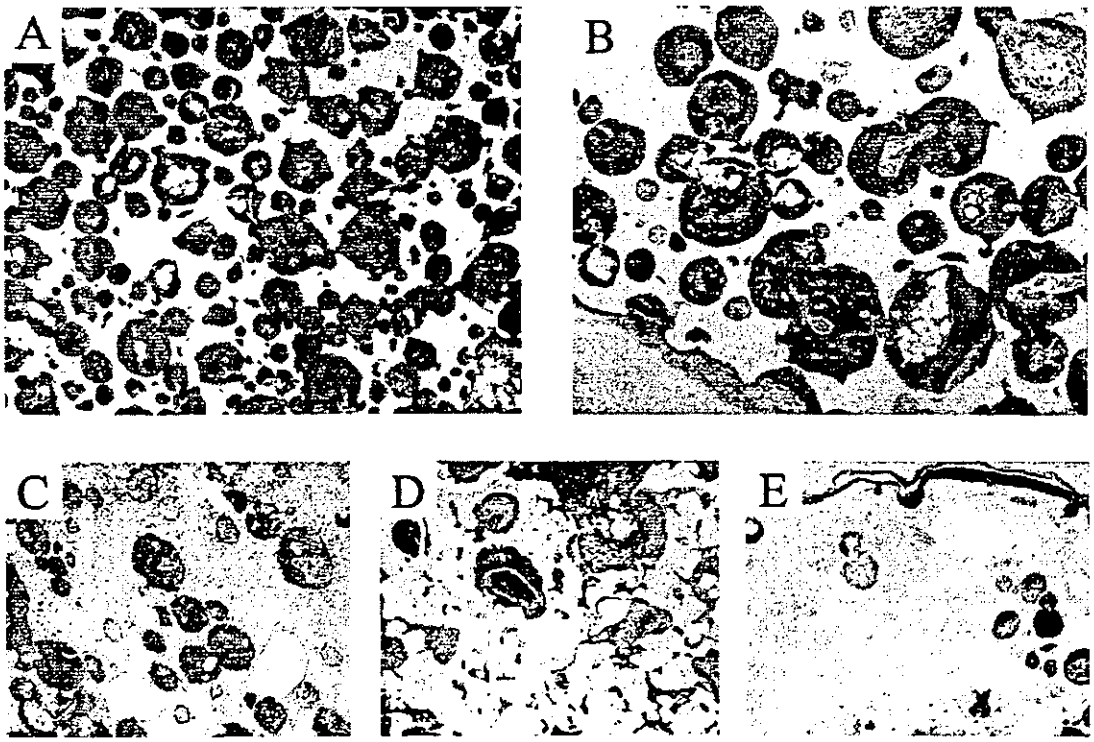


**Figure 3.** Histology of 8-week in vivo implant of various ceramic constructs combined with MMCs and cultured with Dex. (A) HA150/MMCs/cult, (B) HA300/MMCs/cult, (C) HA-A/MMCs/cult, (D) HA-B/MMCs/cult, (E) HA-C/MMCs/cult 8 weeks after implantation. The white area is the ghost of hydroxyapatite ceramic produced by decalcification; the black area is the bone formed in the ceramic pore areas. The HA-A/MMCs/cult, HA-B/MMCs/cult, and HA-C/MMCs/cult showed less bone formation in the pore areas compared with HA150/MMCs/cult and HA300/MMCs/cult. Hematoxylin and eosin staining; original magnification ×40.

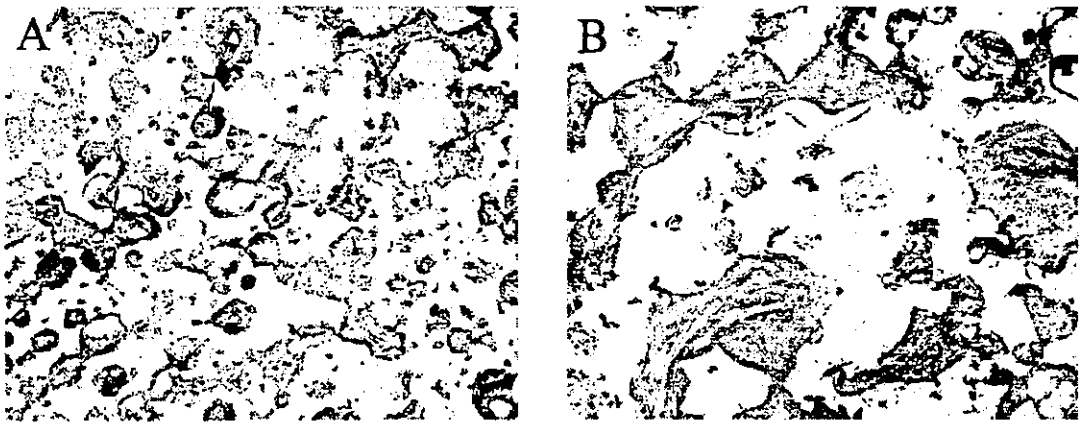


**Figure 4.** Histology of 8-week in vivo implanted IP-CHA without cells. (A) HA150 without cells and (B) HA300 without cells 8 weeks after implantation. In contrast to Figures 2 and 3, the IP-CHA ceramics do not show any bone formation. Hematoxylin and eosin staining; original magnification ×40.

contrast, the ALP activity and osteocalcin contents in the HA150 and HA300 without marrow cells were at basal levels. All of these results confirmed the osteogenic capacity of the constructs of IP-CHA cultured with MMCs. We used two different IP-CHA having two different pore sizes (i.e., HA150 and HA300 had mean pore diameters of 150 and 300 μm, respectively). The ALP and osteocalcin contents of HA150 combined with MMCs were more than those of HA300, meaning that HA150 had superior in vivo osteogenic capacity to that of HA300.

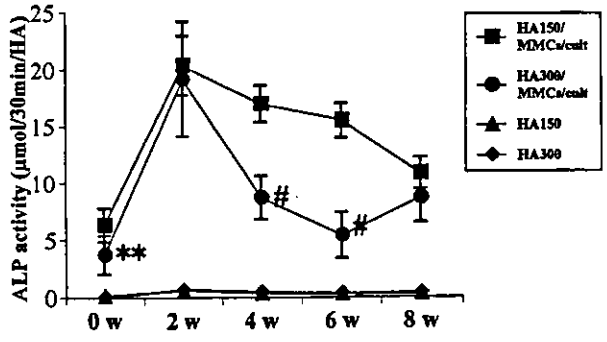


**Figure 5.** In vivo alkaline phosphatase (ALP) activities of implanted HA150/MMCs/cult, HA300/MMCs/cult, HA150, and HA300. IP-CHA was combined with MMCs and cultured with Dex for 2 weeks (HA150/MMCs/cult and HA300/MMCs/cult), then implanted and harvested 0–8 weeks after implantation. HA150 and HA300 without cells were also implanted as controls. The implants were used for ALP assay as described in Materials and Methods. Data are presented as mean ± SD ($n = 5$). $^{**}p < 0.01$, $\#p < 0.0001$ vs. HA150/MMCs/cult. All ALP activities in HA150 and HA300 were significantly lower than those of HA150/MMCs/cult.

*Micro-CT Evaluation of Newly Formed Bone Volume*

To measure the total bone volume in the constructs of IP-CHA (HA150/MMCs/cult and HA300/MMCs/cult) after in vivo implantation, we studied the micro-CT analysis. Figure 7A shows a histological section of the HA300/MMCs/cult construct 8 weeks after implantation; Figure 7B shows a micro-CT image at almost the same level of the histological section of the construct. The micro-CT images show areas having high (white), middle (gray), and low (black) intensities. After matching the histological section with the micro-CT image, we defined the white, gray, and black areas as IP-CHA (HA), newly formed bone (NB), and fibrovascular tissue with fat cells (F), respectively. The software, TRI3D-BON, turned the newly formed bone areas in Figure 7B,

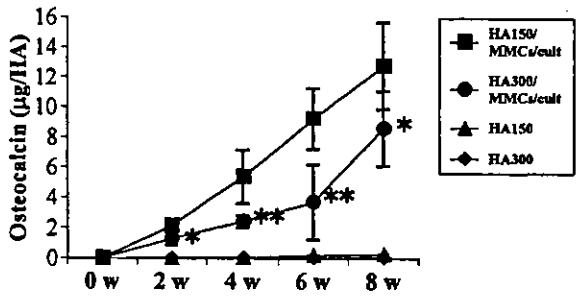


**Figure 6.** Osteocalcin contents of implanted HA150/MMCs/cult, HA300/MMCs/cult, HA150, and HA300. Details of the implants are described in the legend to Figure 5. The implants were used for measuring the osteocalcin contents as described in Materials and Methods. Data are presented as mean ± SD ($n = 5$). $^{*}p < 0.05$, $^{**}p < 0.01$ vs. HA150/MMCs/cult. All osteocalcin contents in HA150 and HA300 were significantly lower than those of HA150/MMCs/cult.

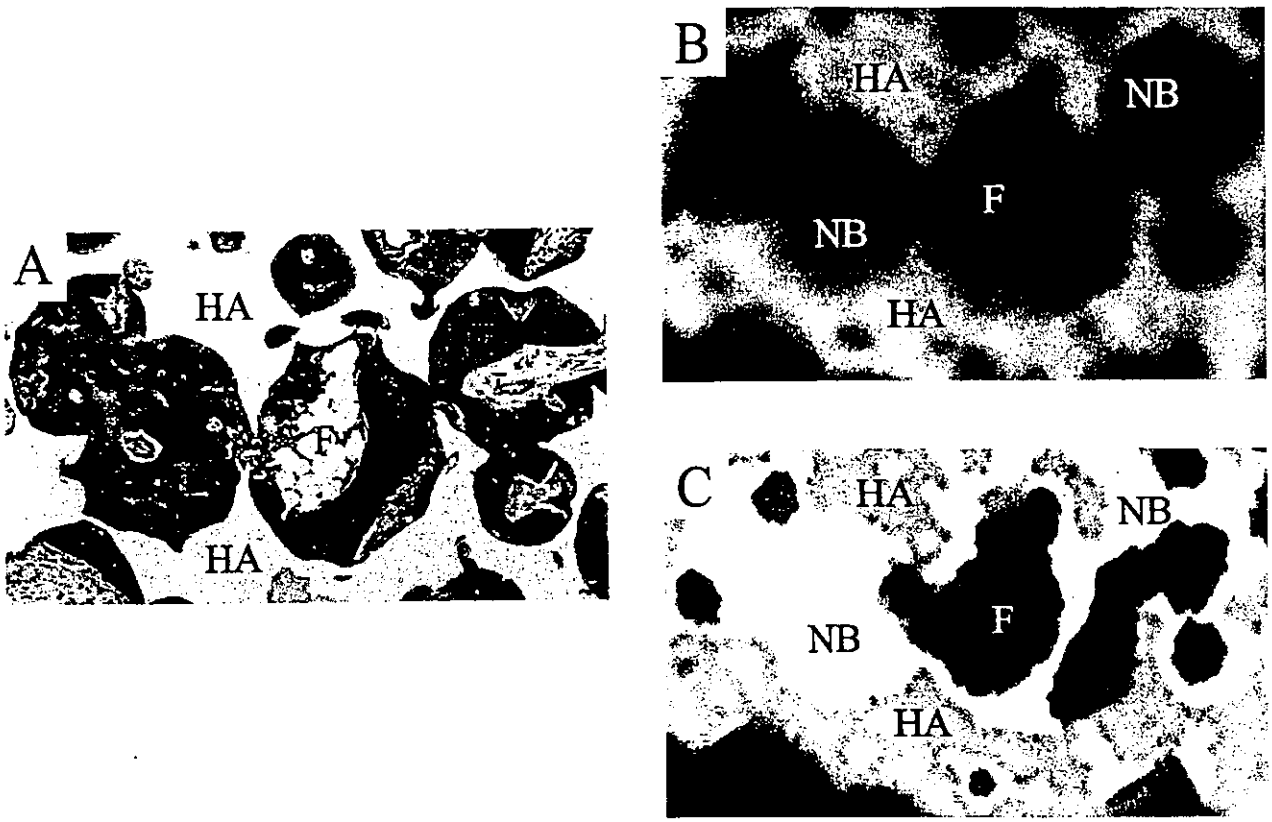


**Figure 7.** Micro-CT evaluation of newly formed bone in IP-CHA. (A) Histological section of HA300/MMCs/cult construct 8 weeks after implantation. Hematoxylin and eosin staining; original magnification ×100. (B) Micro-CT image at almost the same level of the histological section of the construct. (C) Same image of (B) except the gray-colored areas (newly formed bone) are represented in yellow. The micro-CT image (B) depicts the areas having a high (white), middle (gray), and low (black) intensity. By matching the image with the histological section (A), we defined the white, gray, and black areas as IP-CHA (HA), newly formed bone (NB), and soft fibrous tissue including vasculature and fat (F), respectively. Newly formed bone areas in (B) represented as gray areas were turned into yellow by the software program, TRI3D-BON, and illustrated in (C).

represented by the gray areas, into yellow, as shown in Figure 7C. We used the program to measure the yellow areas in each micro-CT section and finally calculated the total volume of yellow-colored areas, which was defined as the total volume of newly formed bone in the constructs. The yellow-colored newly formed bone in HA150/MMCs/cult and HA300/MMCs/cult could be detected 2 weeks after implantation. The bone volumes in both HA150/MMCs/cult and HA300/MMCs/cult gradually increased over time (Fig. 8). We also assembled a three-dimensional (3D) image and evaluated the distribution of newly formed bone at the sagittal section around the center of HA150/MMCs/cult and HA300/MMCs/cult 8 weeks after implantation. As shown in Figure 9, extensive newly formed bone is evident not only in the surface pore areas but also in the center pore areas in both constructs.

The newly formed bone volumes were also measured in the constructs using commercially available synthetic porous hydroxyapatite ceramics (HA-A/MMCs/cult, HA-B/MMCs/cult, and HA-C/MMCs/cult) 8 weeks after implantation. The volumes of these constructs were less than those of HA150/MMCs/cult and HA300/MMCs/cult (Table 1). These data confirmed the histological analyses shown in Figure 3.

## DISCUSSION

The present results confirmed the outstanding role played by IP-CHA in supporting in vitro osteoblastic differentiation of marrow mesenchymal cells (MMCs). More importantly, the ceramics having the cultured cells (MMCs/ceramic/cult constructs) can induce new bone formation after in vivo implantation. Therefore, the constructs having osteogenic capability can be applied in massive bone defects or other cases where there is inferior repair capacity. Thus, the tissue engineering approach is very useful for the regeneration of hard tissue. This approach requires a porous scaffold to make the construct. The scaffold should be biocompatible and have sufficient initial mechanical strength to support the

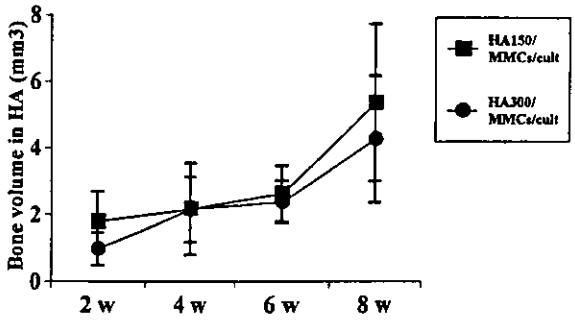


**Figure 8.** Bone volumes in IP-CHA determined by Micro-CT analysis. Temporal changes in bone volumes in HA150/MMCs/cult and HA300/MMCs/cult after implantation. Using the software, TRI3D-BON, we measured the yellow areas in each micro-CT section (Fig. 7C) and finally calculated the total volume of yellow, which was defined as the total volume of the newly formed bone in the constructs. The yellow-colored newly formed bone in HA150/MMCs/cult and HA300/MMCs/cult could be detected 2 weeks after implantation. The bone volumes in both HA150/MMCs/cult and HA300/MMCs/cult gradually increase with the passage of implantation time. There was no significant difference between these two constructs. Data are presented as mean ± SD ($n = 5$).

skeletal structure under weight-bearing conditions. In addition, the scaffold must have a 3D interconnected porous structure to introduce MMCs into the center of the scaffold. The MMCs should differentiate into the osteoblastic lineage.

As we have stated, an interconnected porous structure is very important in the tissue engineering approach. However, currently available commercial synthetic porous ceramics do not possess the ideal interconnected porous structure. To prove the necessity of a porous structure in supporting osteoblastic differentiation, we analyzed the in vivo bone-forming capability of porous ceramics/MMCs constructs by two different morphological approaches: the traditional histological approach and micro-CT analysis. The histological analysis is based on 2D findings of the cut section, and the extent of the bone formation areas may not accurately reflect the bone volume of the constructs because the areas depend on the cutting levels of the sample. In this regard, micro-CT can reconstruct the 3D structure of the HA ceramics, evaluate the 3D distribution of the newly formed bone, and, finally, calculate the bone volume in the ceramics. What is also important is that the analyzed samples can further be utilized for ordinal histological analysis.

As shown in the histological findings of Figures 2 and 3, the constructs of HA-A/MMCs/cult, HA-B/MMCs/cult, and HA-C/MMCs/cult showed new bone formation only in the restricted porous area near the ceramics' surface. In general, as the porosity of porous HA ceramics is higher, the interpore connection rate becomes high. However, to allow cell migration or tissue invasion from pore to pore, theoretically the diameter of the interconnection requires at least 10 μm. In this study, we measured the interpore connection of hydroxyapatite ceramics. Even highly porotic HA-B (70%) have limited interconnections of sufficient size (>10 μm) and the available porosity was as low as 36.7%. This limited interconnection may explain the poor new bone formation by the constructs using porous HA ceramics. In contrast, although the total porosity of IP-CHA was similar to HA-B, the interpore connections of IP-CHA were well controlled between 10 and 100 μm in diameter and the available porosity was from 67% to 70%. The constructs of HA150/MMCs/cult and HA300/MMCs/cult showed extensive bone formation in most pore areas regardless of location (i.e., the bone appeared in both the surface and center pore areas). This uniform appearance of the newly formed bone in most pore areas of the fully open IP-CHA is also revealed by micro-CT analysis. As shown in Figure 9, at the sagittal section of these constructs, excellent bone formation was seen at both the surface and center pore areas. Quantitative micro-CT analysis of bone formed in all constructs showed more bone formation in the HA150/MMCs/cult and HA300/MMCs/cult constructs than in other constructs (Table 1). These two different morphological analyses confirmed that IP-CHA is useful in the tissue engineering approach using MMCs, probably due to its well-organized interconnected porous structure.

The porous structure of IP-CHA was produced by a "foam-gel" technique using a cross-linking polyethyleneimine, enabling control of the pore size and porosity of IP-CHA. In the engineering of bone tissue, the ideal pore size is not clear, although some experiments suggest that a pore size of 200–400 μm is optimal for bone ingrowth (2,5,23). In this study, we used two different pore sizes of IP-CHA: HA150 with a mean pore diameter of 150 μm and HA300 with a mean diameter of 300 μm. Both HA150 and HA300 had the same porosity of 75%. As far as the mechanical properties are concerned, HA150 was superior to HA300 because the compressive strength of HA150 (10 MPa) is higher than that of HA300 (4 MPa) (unpublished data). Therefore, HA150 may be suitable material for bone reconstruction surgery, especially application in weight-bearing areas. An important question that remains, however, is whether the relatively small pore diameter of HA150 can support the osteogenic differentiation of MMCs. To address this point, we measured the level of ALP activity, the early marker of osteoblast differentiation, during in vitro culturing of MMCs in both HA150 and HA300. Both showed high levels of ALP activity with slightly higher levels of HA150 (Fig. 1). We also implanted these ceramics after culturing them with MMCs in Dex for 2 weeks (ceramics/MMCs/cult constructs) and measured

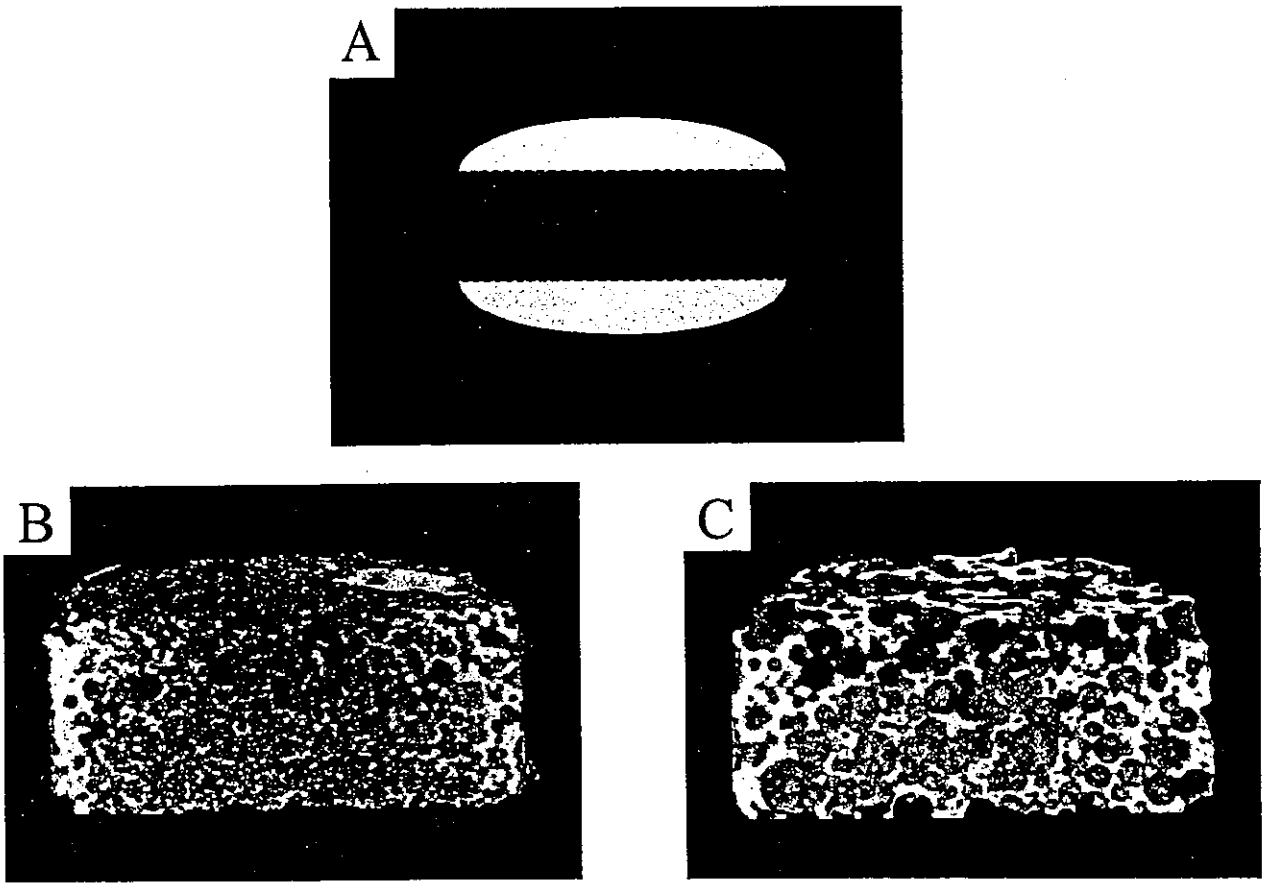


**Figure 9.** Three-dimensional distribution of newly formed bone in IP-CHA determined by Micro-CT analysis. (A) Illustration of the IP-CHA implant. The shaded area is the cross section of the implants. Three-dimensional micro-CT images at the cross section of the HA150/MMCs/cult (B) and HA300/MMCs/cult (C) 8 weeks after implantation. The three-dimensional (3D) image was constructed using the software, TRI3D-BON. The newly formed bone, originally represented in gray, now represented by orange.

the level of ALP activity and osteocalcin contents. Both the ALP activity and the osteocalcin contents of HA150/MMCs/cult were higher than those of HA300/MMCs/cult (Figs. 5 and 6). Micro-CT analysis also confirmed the comparable bone-forming capability of HA150/MMCs/cult to that of HA300/MMCs/cult (Fig. 9, Table 1). These results demonstrated that HA150 with a pore diameter of 150 μm can support the osteoblastic differentiation of MMCs and that the HA150/MMCs construct has more extensive bone-forming capability than does the HA300/MMCs/cult construct. Because of the high degree of mechanical properties of HA150, the HA150/MMCs/cult construct seems to be an ideal tool in bone reconstruction surgery.

**Table 1.** Bone Volumes of Various Constructs Determined by Micro-CT Analysis

| | Bone Volume in Pore Areas ($mm^3$) |
|---|---|
| HA150/MMCs/cult ($n = 5$) | 5.35 ± 2.36 |
| HA300/MMCs/cult ($n = 5$) | 4.26 ± 1.90 |
| HA-A/MMCs/cult ($n = 5$) | 1.88 ± 0.89* |
| HA-B/MMCs/cult ($n = 5$) | 1.57 ± 0.60† |
| HA-C/MMCs/cult ($n = 5$) | 0.52 ± 0.30† |

Values are shown as mean ± SD. $n$: number of implants. There was no statistical difference between HA150/MMCs/cult and HA300/MMCs/cult.
*$p < 0.05$ vs. HA150/MMCs/cult and HA300/MMCs/cult.
†$p < 0.01$ vs. HA150/MMCs/cult and HA300/MMCs/cult.

## CONCLUSIONS

IP-CHA is an excellent ceramic for use in bone tissue engineering because of its fully interconnected porous structure, which allows MMC dispersion and supports their osteogenic differentiation. Ceramics having pores with an average diameter of 150 μm, average interconnecting pore diameter of 40 μm, and 75% porosity (HA150) have a high level of mechanical strength. When cultured with MMCs for 2 weeks in vitamin C, glycerophosphate, and dexamethasone, HA150 has extensive in vivo capability for forming new bone. There-

fore, in combination with MMCs culture, HA150 could be an extremely useful tissue engineering material in bone reconstruction surgery.

*ACKNOWLEDGMENTS: The authors thank Toshiba Ceramics Co., Ltd. for supplying materials and technical assistance, and K. Asai for histological technical assistance. This work was done by Three-Dimensional Tissue Module Project, METI (a Millennium Project).*

## REFERENCES

1. Ayers, R. A.; Simske, S. J.; Nunes, C. R.; Wolford, L. M. Long-term bone ingrowth and residual microhardness of porous block hydroxyapatite implants in humans. J. Oral Maxillofac. Surg. 56:1297–1301; 1998.
2. Boyan, B. D.; Hummert, T. W.; Dean, D. D.; Schwartz, Z. Role of material surfaces in regulating bone and cartilage cell response. Biomaterials 17:137–146; 1996.
3. Bucholz, R.; Carlton, A.; Holmes, R. Interporous hydroxyapatite as a bone graft substitute in tibial plateau fractures. Clin. Orthop. 240:53–62; 1988.
4. de Groot, K. Bioceramic consisting of calcium phosphate salts. Biomaterials 1:47–50; 1980.
5. Dennis, J. E.; Haynesworth, S. E.; Young, R. G.; Caplan, A. I. Osteogenesis in marrow-derived mesenchymal cell porous ceramic composites transplanted subcutaneously: Effect of fibronectin and laminin on cell retention and rate of osteogenic expression. Cell Transplant. 1:23–32; 1992.
6. Dohi, Y.; Ohgushi, H.; Tabata, S.; Yoshikawa, T.; Dohi, K.; Moriyama, T. Osteogenesis associated with bone Gla protein gene expression in diffusion chambers by bone marrow cells with demineralized bone matrix. J. Bone Miner. Res. 7:1173–1180; 1992.
7. Jarcho, M. Calcium phosphate ceramics as hard tissue prosthetics. Clin. Orthop. 157:259–278; 1981.
8. Kato, K.; Aoki, H.; Tabata, T.; Ogiso, M. Biocompatibility of apatite ceramics in mandibles. Biomater. Med. Devices Artif. Organs 7:291–297; 1979.
9. Maniatopoulos, C.; Sodek, J.; Melcher, A. H. Bone formation in vitro by stromal cells obtained from marrow of young adult rats. Cell Tissue Res. 254:317–330; 1988.
10. Nakano, K.; Harata, S.; Suetsuna, F.; Araki, T.; Itoh, J. Spinous process-splitting laminoplasty using hydroxyapatite spinous process spacer. Spine 17:S41–S43; 1992.
11. Ohgushi, H.; Goldberg, V. M.; Caplan, A. I. Heterotopic osteogenesis in porous ceramics induced by marrow cells. J. Orthop. Res. 7:568–578; 1989.
12. Ohgushi, H.; Goldberg, V. M.; Caplan, A. I. Repair of bone defects with marrow and porous ceramic. Acta Orthop. Scand. 60:334–339; 1989.
13. Ohgushi, H.; Okumura, M. Osteogenic capacity of rat and human marrow cells in porous ceramics. Acta Orthop. Scand. 61:431–434; 1990.
14. Ohgushi, H.; Dohi, Y.; Tamai, S.; Tabata, S. Osteogenic differentiation of marrow stromal stem cells in porous hydroxyapatite ceramics. J. Biomed. Mater. Res. 27:1401–1407; 1993.
15. Ohgushi, H.; Dohi, Y.; Katuda, T.; Tamai, S.; Tabata, S.; Suwa, Y. In vitro bone formation by rat marrow cell culture. J. Biomed. Mater. Res. 32:333–340; 1996.
16. Ohgushi, H.; Dohi, Y.; Yoshikawa, T.; Tamai, S.; Tabata, S.; Okunaga, K.; Shibuya, T. Osteogenic differentiation of cultured marrow stromal stem cells on the surface of bioactive glass ceramics. J. Biomed. Mater. Res. 32:341–348; 1996.
17. Ohgushi, H.; Yoshikawa, T.; Nakajima, H.; Tamai, S.; Dohi, Y.; Okunaga, K. Al2O3 doped apatite-wollastonite containing glass ceramic provokes osteogenic differentiation of marrow stromal stem cells. J. Biomed. Mater. Res. 44:381–388; 1999.
18. Ohgushi, H.; Caplan, A. I. Stem cell technology and bioceramics: From cell to gene engineering. J. Biomed. Mater. Res. 48:–913–927; 1999.
19. Reddi, A. H.; Sullivan, N. S. Matrix-induced endochondral bone differentiation: Influence of hypophysectomy, growth hormone, and thyroid-stimulating hormone. Endocrinology 107:1291–1299; 1980.
20. Tamai, N.; Myoui, A.; Tomita, T.; Nakase, T.; Tanaka, J.; Ochi, T.; Yoshikawa, H. Novel hydroxyapatite ceramics with an interconnective porous structure exhibit superior osteoconduction in vivo. J. Biomed. Mater. Res. 59:110–117; 2002.
21. Uchida, A.; Araki, N.; Shinto, Y.; Yoshikawa, H.; Kurisaki, H.; Ono, K. The use of calcium hydroxyapatite ceramic in bone tumor surgery. J. Bone Joint Surg. Br. 72: 298–302; 1990.
22. van Blitterswijk, C. A.; Hesseling, S. C.; Grote, J. J.; Koerten, H. K.; deGroot, K. The biocompatibility of hydroxyapatite ceramics: A study of retrieved human middle ear implants. J. Biomed. Mater. Res. 24:433–453; 1990.
23. Whang, K.; Thomas, C. H.; Healy, K. E.; Nuber, G. A novel method to fabricate bioabsorbable scaffolds. Polymer 36:837–842; 1995.
24. Yoshikawa, T.; Ohgushi, H.; Okumura, M.; Tamai, S.; Dohi, Y.; Moriyama, T. Biochemical and histological sequences of membranous ossification in ectopic site. Calcif. Tissue Int. 50:184–188; 1992.
25. Yoshikawa, T.; Ohgushi, H.; Tamai, S. Immediate bone forming capability of prefabricated osteogenic hydroxyapatite. J. Biomed. Mater. Res. 32:481–492; 1996.

ELSEVIER

Journal of Orthopaedic Research 22 (2004) 1248–1253

Journal of Orthopaedic Research

www.elsevier.com/locate/orthres

# Effects of rotation on measurement of lower limb alignment for knee osteotomy

Hideo Kawakami [a,*], Nobuhiko Sugano [b], Kazuo Yonenobu [c], Hideki Yoshikawa [b], Takahiro Ochi [a], Asaki Hattori [d], Naoki Suzuki [d]

[a] *Department of Medical Robotics and Image Sciences, Division of Robotic Therapy, Osaka University Graduate School of Medicine, 2-2 Yamadaoka, Suita, Osaka 565-0871, Japan*

[b] *Department of Orthopaedic Surgery, Osaka University Graduate School of Medicine, 2-2 Yamadaoka, Suita, Osaka 565-0871, Japan*

[c] *Department of Orthopaedic Surgery, Osaka-Minami National Hospital, Osaka 586-0008, Japan*

[d] *Institute for High Dimensional Medical Imaging, Jikei University School of Medicine, Komae, Tokyo 201-8601, Japan*

**Abstract**

The purposes of this study were to clarify the effects of rotation on two-dimensional measurement of lower limb alignment for knee osteotomy using a three-dimensional method and to determine whether this 3-D simulation method could help with planning of knee osteotomy. We developed computer software to calculate femorotibial angle (FTA) and hip–knee–ankle angle (HKA) and simulate knee osteotomy from a CT-based 3-D bone model of the lower limb. Lower limb rotation on anteroposterior long-standing radiographs was measured by superimposing the 3-D bone models. Changes in alignment with limb rotation were calculated using the software. FTA after virtual closed-wedged osteotomy was measured for a hypothetical case of a rotation error of the osteotomy plane in reattaching the proximal cutting surface to the distal cutting surface. For 31 varus knees in 20 patients with medial compartment arthritis, the mean rotation angle, relative to the epicondylar axis, with variable limb position was 7.4 ± 3.9° of internal rotation (mean ± SD), ranging from 8° of external rotation to 14° of internal rotation; the mean changes in FTA and HKA were 3.5 ± 2.2° (range, 0.4–8.6) and 1.6 ± 1.3° (range, 0.2–4.9), respectively. The FTA "flexion angle" (lateral view alignment from neutral AP) and the absolute HKA "flexion angle" correlated with the change in FTA and HKA with limb rotation, respectively (FTA, $R = 0.999$; HKA, $R = 0.993$). The mean change in FTA after virtual closed-wedged osteotomy was 3.2° for internal and external 10° rotation errors in reattaching the osteotomy plane. Rotation may affect measurement of lower limb alignment for knee osteotomy, and 3-D methods are preferable for surgical planning.


*Keywords:* Lower limb alignment; High tibial osteotomy; 3-D CT simulation

## Introduction

High tibial osteotomy (HTO) is a treatment option for medial compartment osteoarthritis (OA) of the knee. The goal of HTO is to reduce abnormal loads. The expected survival rate is approximately 85% at 5 years and 60% at 10 years [5,7,9,10,18,19,23]. Factors that affect outcome include operative factors [5,17,23] and patient factors, including pre-operative grade of OA, age, obesity, and range of motion [3,9]. Measurement of lower limb alignment on plain radiographs is used as an alternative indicator of the loading imbalance because of difficulties in measuring the load on the medial and lateral surfaces of the knee joint non-invasively.

Correction of lower limb alignment is one of the most critical operative factors; appropriate correction yields good to excellent results (success rate of 87–100% at 5–10 years), but inappropriate correction (under- or over-correction) yields poor results (success rate of 26–63% at 5–10 years) [5,7,19]. The recommended alignment varies widely, with recommended hip–knee–ankle angles (HKA) ranging from 2° to 7° [5,7,10,13] and femorotibial angles (FTA) ranging from 164° to 175° [9,12,15,21,23]. Conventionally, pre-operative lower limb alignment has been measured two-dimensionally on AP long-standing radiographs of the lower limb, but variability of rotation in positioning of the limb during radiography can affect

* Corresponding author. Tel.: +81-6-6879-3552; fax: +81-6-6879-3869.
*E-mail address:* hkawakami-osk@umin.ac.jp (H. Kawakami).

0736-0266/$ - see front matter © 2004 Orthopaedic Research Society. Published by Elsevier Ltd. All rights reserved.
doi:10.1016/j.orthres.2004.03.016

measurements. The effects of rotation on lower limb alignment have been reported [14,20,22], but based only on theoretical assessments.

Intra-operative osteotomy plane rotation cannot be simulated using two-dimensional radiographs. Thus, pre-operative planning based on AP radiographs and an intra-operative technique with osteotomy plane rotation could cause inappropriate correction of lower limb alignment. To clarify the effects of rotation on knee osteotomy and to facilitate pre-operative planning using 3-D images, we developed computer software that measures lower limb alignment in 3-D images and simulates knee osteotomy. In the present study, we examined 31 knees in twenty patients with medial compartment OA in varus knees to clarify important issues regarding alignment and planning.

## Materials and methods

The patients were 7 men and 13 women ranging in age from 31 to 85 years (mean, 64.8 years). Using the Kellgren and Lawrence radiographic classification of OA [11], 11 knees (36%) had grade 2, indicating osteophytes and possible joint space narrowing, 15 knees (48%) had grade 3, indicating moderate multiple osteophytes, definite joint space narrowing, some sclerosis, and possible bone contour deformity, and 5 knees (16%) had grade 4, indicating large osteophytes, marked joint space narrowing, severe sclerosis, and definite bone contour deformity. There were no severe degenerative changes in the patellofemoral or lateral femorotibial articulations. The average Knee Society score [8] was 53 ± 22 points, and the average functional score was 73 ± 21 points. All patients were completely informed about this study and consented to the examination.

AP long-standing radiographs of the lower limb were taken while the radiologist carefully attempted to position the patella facing forward. Transverse images from the proximal end of the femur to the distal end of the tibia were obtained using a helical CT scanner. To match the position during stance, the positioning during the scan was with the knee in full extension and the ankle joint at 90° of flexion, with an ankle braced in the supine position. Slice thickness and slice pitch were: 3 mm for the femoral head; 10 mm for the femoral shaft; 2 mm for the segment from 10 mm above the femoral epicondyles to the top of the tibial eminence; 1 mm for the segment from the tibial eminence to 10 mm below the tibial eminence; 2 mm for the segment from 10 mm below the tibial eminence to the tibial tuberosity; 10 mm for the tibial shaft; and 2 mm for the segment from 10 mm above the ankle joint to 10 mm below the ankle joint.

We reconstructed 3-D skeletal models of the femur, tibia, and patella from the CT images, using surface rendering software (Analyze PC 3.0, Mayo Foundation, Rochester, MN). To define the knee joint coordinates, 4 landmark points were plotted on the 3-D surface models. The first point (F) was the center of the femoral head, which was designated as the center of the best-fit sphere. The second and third points (LE and ME) were the top of the medial and lateral femoral epicondyles, respectively. The fourth point (TD) was the centroid of multiple points on the distal tibial joint surface that were surrounded by a manually drawn circle. Based on these points, the coordinates of the knee joint were defined to indicate the front of the knee (neutral position) and the axis of the lower limb rotation (Fig. 1). The vertical $Z$-axis was defined as the line through F and TD. This line is sometimes referred to as the initial mechanical axis of the lower extremity. A transverse plane, TP, was defined as the plane perpendicular to $Z$ (the mechanical axis of the lower extremity) and passing through the medial epicondyle; i.e., including the point ME. The point LEp was defined as the projection of the lateral epicondyle (LE) onto this transverse plane. LEp was projected along a line parallel to $Z$, extending from LE to the transverse plane TP. The $X$-axis, representing a neutral medial to lateral direction, was defined as the axis

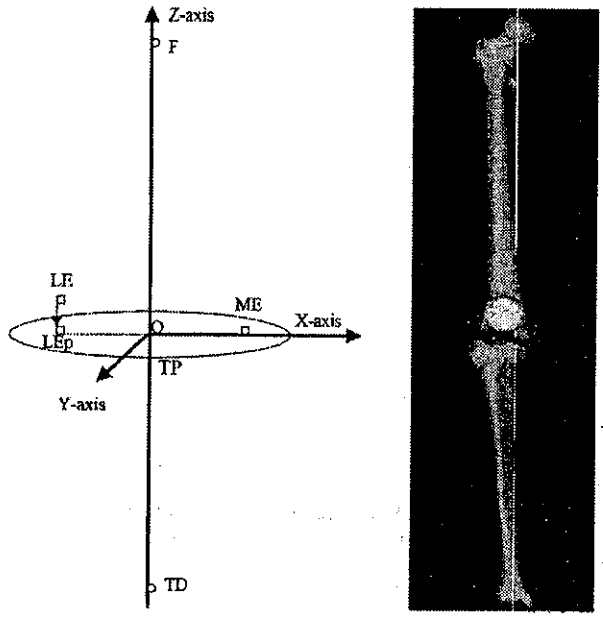


Fig. 1. The coordinates defining the front of the knee. $Z$-axis, the axis of lower limb rotation; F, the center of the femoral head; ME, the medial epicondyle; LE, the lateral epicondyle; TD, the center of gravity of the distal tibia joint surface.

containing the line ME-LEp; i.e., the epicondylar projection. The $X$-axis was perpendicular to $Z$, contained the transverse plane, was parallel to ME-LEp, and (being an axis) defined the origin of $Z$. The $Y$-axis passed through the intersection of axes $X$ and $Z$ and was perpendicular to each. The $Y$-axis was therefore a neutral AP axis of the distal femur, and for our purposes, was the neutral AP vector for the knee itself. The front of the knee was defined from the transepicondylar axis, because the transepicondylar axis is a reliable rotational landmark not affected by distortion of the femoral condyles [2].

To measure lower limb axial alignment from 3-D images, we developed computer software that projected the 3-D models on a two-dimensional $XZ$ plane (the plane of the mechanical axis $Z$ and the projected epicondylar axis EM-ELp) and calculated the angle. FTA and HKA were used as indices of lower limb alignment [1,16]. FTA is the lateral angle at the intersection between the femoral shaft axis and the tibial shaft axis, and HKA is the medial angle deviation from 180° at the intersection between the mechanical axes of the femur and tibia, plus for valgus alignment and minus for varus alignment.

To measure FTA from 3-D images, the femoral shaft axis was defined as the line through the centroid of multiple points on the femoral transverse sections at 25% of the femoral length below the center of the femoral head and at 20% of the femoral length above the point M on the epicondylar axis EM-ELp. The point M was the intersection of the epicondylar axis EM-ELp and the line perpendicular to EM-ELp that passes through the center of the femoral head. The femoral length was defined as the distance from the center of the femoral head to the point M. The tibial shaft axis was defined as the line through the centroid of multiple points on the tibial transverse sections at 20% of the tibial length below the proximal end of the tibia and at 20% of the tibial length above the distal end of the tibia. The tibial length was defined as the distance from the midpoint between the tips of the medial and lateral tibial spines and the centroid of the multiple points on the distal tibia joint surface.

To measure HKA from 3-D images, the mechanical axis of the femur was defined as the line through the center of the femoral head and the midpoint between the tips of the medial and lateral tibial spines, and the mechanical axis of the tibia was defined as the line through the midpoint between the tips of the medial and lateral tibial spines and the centroid of the multiple points on the distal tibia joint surface.

To study the variable positioning of the limb by the radiologist, the lower limb rotation on the AP long-standing radiographs was measured by superimposing the 3-D bone models on the radiograph, taking into account the relative position of the patellar and femoral outlines obtained from the radiographs. Next, the 3-D model was rotated around the *Z*-axis in the computer simulation. The relative positions of the patella and femur in the models were superimposed on the patellar and femoral outlines from the radiograph. The relative positions of the patella and femur in the models were matched to the patellar and femoral outlines of the radiograph by rotating the models in the computer simulation. We also measured the rotation angle of the models from the neutral position (the *Y*-axis in the knee coordinate system).

The 3-D bone model was rotated from the neutral position to the maximum rotation obtained from radiographic measurements for all patients. Based on limb rotation in the computer simulation, possible changes in FTA and HKA with limb rotation were calculated using the computer software.

To study correlations between apparent axial deformity of the lower limb and variation in FTA and HKA with limb rotation, we measured and analyzed FTA and HKA on AP long-standing radiographs of the lower limb, the "flexion angle" of FTA and HKA calculated by the computer software, and the change in FTA and HKA with limb rotation. The "flexion angle" was defined as the angle from a lateral view of those axes, specifically normal to the neutral AP, viewed along the line of the ML rotational axis of the femur. The "flexion angles" of FTA and HKA were calculated with lateral projections of FTA and HKA using the computer software. The changes in FTA and HKA were calculated by the reduction of the minimum angle from the maximum angle in the range of rotation from radiographic measurements. Polynomial regression models were used to check the relationships between the axis deformity of the lower limb and the changes in FTA and HKA with limb rotation.

We developed computer software that simulates knee osteotomy by cutting the bone models in any plane, removing the wedged bone, and reattaching or opening the surfaces in the coordinate of the tibia. The coordinate of the tibia was defined as follows. The points Mt and Lt on medial and lateral joint surfaces of the proximal tibia were defined as the centroid of multiple points on the joint surface that were surrounded by a manually drawn circle. The line through the points Mt and Lt was defined as the joint line of the proximal tibia joint surface. The *Zt*-axis, representing the vertical, was defined as the line through TD and the mid-point of MT and LT. The transverse plane TPt was defined as the plane perpendicular to the *Zt*-axis and passing through the point Mt. The *Xt*-axis was the line through the point Mt and the intersection of the *Zt*-axis and the transverse plane TPt. The *Yt*-axis was perpendicular to the *Zt*- and *Xt*-axis.

Using this computer software, we simulated knee osteotomy to help with pre-operative planning on the computer display. To examine the effect of intra-operative osteotomy plane rotation on changes in axial alignment, we simulated closed-wedge HTO. The osteotomy plane was parallel to the tibial articular surface at 25 mm below the joint line through the point Mt and the point Lt. The target post-operative alignment was set at 4° of HKA. Rotation error of the osteotomy plane may affect determination of the direction of the cutting plane and reattachment of the cutting surfaces. FTA and HKA after virtual knee osteotomy were measured for a hypothetical case of internal and external 15° osteotomy plane rotation in the cutting plane direction of the proximal tibia. This osteotomy plane was twisted around the *Zt*-axis. FTA and HKA after virtual knee osteotomy were measured for a hypothetical case of internal and external 15° osteotomy plane rotation in reattaching the proximal cutting surface to the distal cutting surface. This osteotomy plane was twisted around the shaft parallel to the *Zt*-axis through the point of the medial wedge on the osteotomy plane (Fig. 2).

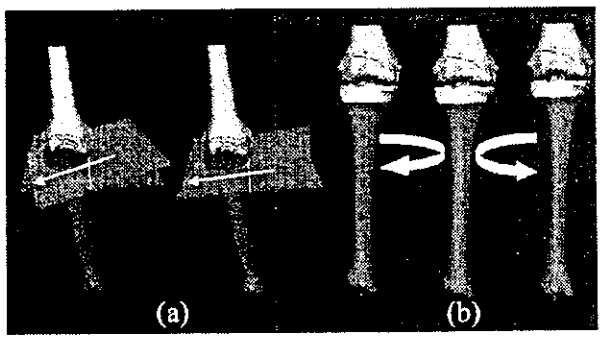


Fig. 2. Operative simulation of HTO: (a) osteotomy plane rotation in the cutting plane direction of the proximal tibia. (b) Osteotomy plane rotation in reattaching the proximal cutting surface to the distal cutting surface.

## Results

The mean FTA and HKA on AP long-standing radiographs of the lower limb was 183.5 ± 5.5° (mean ± SD; range, 178–205) and −9.2 ± 5.6° (range, −30 to −4), respectively. The mean rotation angle with variable limb position was 7.4 ± 3.9° of internal rotation, ranging from 8° of external rotation to 14° of internal rotation from the neutral position (the *Y*-axis in the coordinate system of the knee). Within the range of rotation angles, we calculated the difference between the minimum axial alignment angle and the maximum axial alignment angle. The mean change in FTA with limb rotation was 3.5 ± 2.2° (range, 0.4–8.6), and the mean change in HKA was 1.6 ± 1.3° (range, 0.2–4.9).

The change in FTA with limb rotation increased as the "flexion angle" of FTA increased (Table 1 and Fig. 3a). The change in HKA with limb rotation increased as the absolute "flexion angle" of HKA increased (Fig. 3b). A positive correlation was found between the "flexion angle" of FTA (FFTA) and the change in FTA with lower limb rotation (CFTA), with a straight regression line (CFTA = 0.386, FFTA−2.696) and a correlation coefficient of 0.999 (Fig. 3c). A positive correlation existed between the absolute "flexion angle" of HKA (AFHKA) and the change in HKA with lower limb rotation (CHKA), with a straight regression line (CHKA = 0.381, AFHKA+0.009) and a correlation coefficient of 0.993 (Fig. 3d). No significant correlation was found between alignment on AP radiographs and the change in alignment with lower limb rotation ($R = 0.357$ for FTA; $R = 0.319$ for HKA).

For the hypothetical case of internal and external 5°, 10° and 15° osteotomy plane rotation, the change in FTA was 0.2 ± 0.1°, 0.4 ± 0.3° and 0.8 ± 0.4°, respectively, and the change in HKA was 0.2 ± 0.1°, 0.4 ± 0.2° and 0.7 ± 0.3°, respectively. Closed-wedged osteotomy was also simulated for a hypothetical case of osteotomy plane rotation in reattaching the proximal cutting surface to the distal cutting surface. For the hypothetical case of internal and external 5°, 10° and 15° osteotomy plane rotation, the change in FTA was 1.6 ± 0.6°, 3.2 ± 1.1° and 4.8 ± 1.7°, respectively, and the change in HKA was 0.9 ± 0.5°, 1.9 ± 1.0° and 2.8 ± 1.5°, respectively.

Table 1
FTA and HKA on AP radiographs, the "Flexion angle" of FTA and HKA calculated using the computer software, and the change in FTA and HKA with lower limb rotation (31 varus knees of 20 patients)

| Knee number | Gender[a] | FTA on AP radiograph | "Flexion angle" of FTA[b] | Change in FTA with limb rotation[c] | HKA on AP radiograph | "Flexion angle" of HKA[b] | Change in HKA with limb rotation[c] |
|---|---|---|---|---|---|---|---|
| 1 | F | 178.0 | 2.6 | 0.9 | −5.0 | 5.9 | 2.2 |
| 2 | F | 178.0 | 5.9 | 2.2 | −4.0 | 2.6 | 0.9 |
| 3 | F | 178.0 | 7.2 | 2.7 | −4.0 | 1.8 | 0.6 |
| 4 | F | 179.0 | 6.3 | 2.4 | −4.0 | 2.9 | 1.0 |
| 5 | F | 179.0 | 5.4 | 2.0 | −5.0 | 4.7 | 1.8 |
| 6 | M | 179.0 | 15.9 | 6.1 | −4.0 | −6.7 | 2.6 |
| 7 | M | 180.0 | 2.5 | 0.9 | −8.0 | 6.3 | 2.3 |
| 8 | F | 180.0 | 11.6 | 4.4 | −6.0 | −2.2 | 0.9 |
| 9 | M | 181.0 | 7.6 | 2.9 | −7.0 | 1.2 | 0.3 |
| 10 | M | 181.0 | 17.5 | 6.8 | −7.0 | −7.4 | 3.0 |
| 11 | M | 181.0 | 10.4 | 4.1 | −7.0 | −1.9 | 0.9 |
| 12 | M | 181.0 | 12.3 | 4.7 | −8.0 | −2.2 | 1.0 |
| 13 | F | 181.0 | 8.8 | 3.4 | −8.0 | 1.9 | 0.6 |
| 14 | F | 182.0 | 10.2 | 4.0 | −7.0 | −0.6 | 0.4 |
| 15 | M | 182.0 | 8.5 | 3.3 | −9.0 | 2.8 | 0.9 |
| 16 | M | 182.0 | 3.0 | 1.1 | −9.0 | 7.3 | 2.7 |
| 17 | M | 182.0 | 7.4 | 2.8 | −5.0 | −0.3 | 0.2 |
| 18 | M | 182.0 | 20.8 | 8.0 | −6.0 | −11.4 | 4.5 |
| 19 | F | 182.0 | 22.4 | 8.6 | −7.0 | −12.6 | 4.9 |
| 20 | F | 183.0 | 3.4 | 1.3 | −11.0 | 3.9 | 1.3 |
| 21 | F | 183.0 | 10.7 | 4.0 | −5.0 | −0.3 | 0.2 |
| 22 | F | 185.0 | 10.7 | 4.1 | −11.0 | −1.8 | 0.8 |
| 23 | F | 185.0 | 12.1 | 4.6 | −11.0 | −4.8 | 1.9 |
| 24 | M | 186.0 | 3.9 | 1.6 | −10.0 | 6.7 | 2.3 |
| 25 | F | 186.0 | 6.0 | 2.4 | −15.0 | 2.4 | 0.7 |
| 26 | F | 187.0 | 0.7 | 0.4 | −11.0 | 7.9 | 2.8 |
| 27 | F | 187.0 | 3.3 | 1.4 | −11.0 | 4.8 | 1.6 |
| 28 | F | 188.0 | 7.4 | 2.9 | −14.0 | −0.6 | 0.4 |
| 29 | F | 188.0 | 5.9 | 2.3 | −12.0 | 0.8 | 0.2 |
| 30 | F | 196.0 | 9.7 | 3.9 | −23.0 | −0.2 | 0.6 |
| 31 | F | 205.0 | 20.4 | 8.0 | −30.0 | −10.9 | 4.5 |

[a] F: female, M: male.
[b] "Flexion angle" was defined as the angle from a lateral view of AP neutral position.
[c] Change in limb alignment was calculated by the reduction of the minimum angle from the maximum angle within the range of rotation from the neutral position.

## Discussion

In a study of the effect of rotation on lower limb axial alignment, Wright et al. [22] found that limb rotation of 10° internally and externally had only a small effect on FTA in radiographs of amputated lower extremities. Swanson et al. [20] reported that limb rotation of 10° internally and externally had a statistically significant effect on FTA in radiographs of Sawbone extremity models with severe valgus or varus deformity. Krackow et al. [14] analyzed the effect of flexion and rotation on varus and valgus deformity by calculating the assumed leg deformity. With rotation and flexion of up to 10° each, the artifactual contributions to axial deformity were very small at less than 2° of HKA, but with flexion and rotation of 10–20° each, the changes became significant at up to 7.4° of HKA.

These previous studies did not include clinical patients and were only theoretical assessments. The present study involved 31 varus knees of patients with medial compartment OA. Radiographic measurements were obtained under clinical conditions, and the mean change in FTA and HKA within the range of rotation was 3.5° (range, 0.4–8.6) and 1.6° (range, 0.2–4.9), respectively. The present results show a measurement error that may occur in assessment of lower limb alignment in clinical situations. When measuring lower limb alignment and planning knee osteotomy on radiographs, the extent of variation of lower limb alignment with limb rotation should be considered.

In previous studies, it was unclear what factors were involved in changes in lower limb alignment with limb rotation. In the present study, we examined the "flexion angle" of FTA and the "flexion angle" of HKA. The "flexion angle" was defined as the angle from a lateral view of those axes and was considered to be the flexion angle of the knee during radiography. The "flexion angle" of FTA and the absolute "flexion angle" of HKA

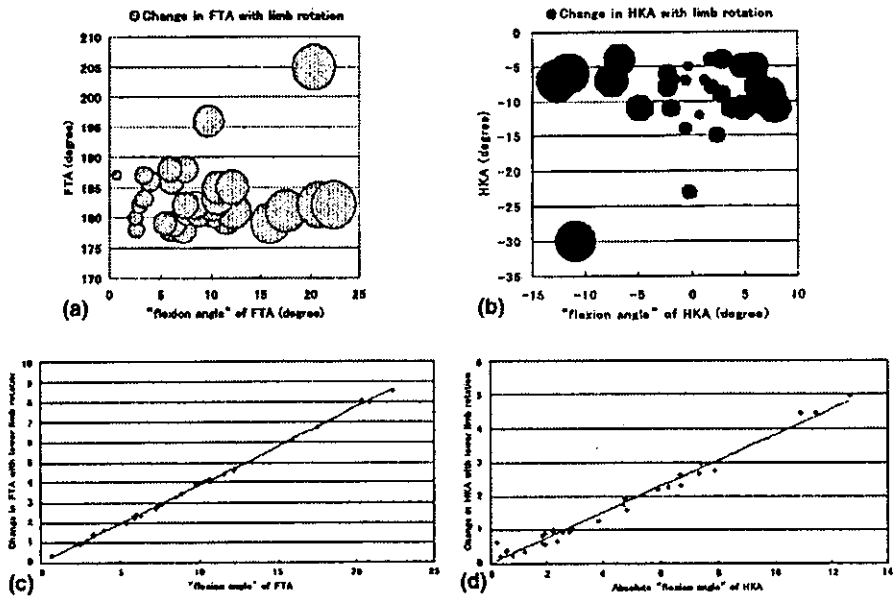


Fig. 3. Relationship between FTA and HKA on AP radiograph, the "flexion angle" of FTA and HKA calculated using the computer software, and the change in FTA and HKA with limb rotation. (a) The change in FTA increased as the "flexion angle" of FTA increased. (b) The change in HKA increased as the absolute "flexion angle" of HKA increased. (c) The linear regression line between the "flexion angle" of FTA and the change in FTA with lower limb rotation. (d) The linear regression line between the absolute "flexion angle" of HKA and the change in HKA with lower limb rotation.

were highly correlated with changes in FTA and HKA with limb rotation, respectively. However, no significant correlation was found between alignment on AP radiographs and the change in alignment with lower limb rotation. Thus, our findings show that the "flexion angle" of the knee during radiography was the main source of the effect of rotation on limb alignment, rather than the varus deformity of the knee on clinical radiographs.

In the present study, the effect of rotation on limb alignment increased as the "flexion angle" increased. The "flexion angle" of FTA tended to be larger than the absolute "flexion angle" of HKA because the center of the femoral head (including the line of HKA) is always anterior to the femoral shaft axis in anteversion of the femoral head and because the midpoint between the tibial spines (including the line of HKA) is often posterior to femoral shaft axis. The mean change in FTA with limb rotation was greater than the mean change in HKA with limb rotation. Thus, HKA should be used for assessment of lower limb alignment on radiographs when the "flexion angle" of the lower limb alignment is large.

Previously, two groups reported on computer-assisted knee osteotomy. Chao et al. developed a 2-D rigid-body spring model to simulate the forces across the articular surfaces [4]. Ellis et al. used a 3-D pre-surgical planner and an intra-operative guidance system [6]. The 3-D pre-surgical planner provides a 3-D model, but only around the knee joint. We developed computer software that simulates knee osteotomy and calculates axial alignment over the full length of the lower extremities. The present 3-D system allowed us to precisely analyze pre- and post-operative lower limb alignment. We were able to simulate the changes in FTA and HKA with limb rotation and intra-operative osteotomy plane rotation. This system proved useful for pre-operative planning of knee osteotomy.

No clinical reports exist concerning the effect of osteotomy plane rotation on axial alignment in knee osteotomy. The present study simulated the effect of osteotomy plane rotation on lower limb alignment for the direction of the osteotomy plane and reattachment of the osteotomy plane within internal and external rotation of 15°. The rotation in reattachment of the osteotomy plane affected lower limb alignment, whereas the rotation in the direction of the osteotomy plane did not. In the case of internal and external 10° rotations in reattaching the proximal cutting surface to the distal cutting surface, the mean changes in FTA and HKA were 3.2° and 1.9°, respectively. Thus, intra-operative technique with rotation factor can affect lower limb alignment after knee osteotomy. The present 3-D method is useful for precise assessment of lower limb alignment after knee osteotomy.

Bony landmarks for determining the 3-D coordinate of the lower limb are not easily identified or repeatable. In the present system, we obtained thin-slice CT images around the landmark points to facilitate identification. To examine measurement accuracy of lower limb alignment using this 3-D method, one orthopaedic surgeon plotted the six landmarks, and five trials were performed